A multi-port non-isolated bidirectional DC-DC converter

Sepideh Bahravar, Karim Abbaszadeh* and Javad Olamaei

Department of Electrical and Computer Engineering,
Islamic Azad University,
South Tehran Branch, Tehran, Iran
Email: st_s_bahravar@azad.ac.ir
Email: k_abbaszadeh@azad.ac.ir
Email: j_olamaei@azad.ac.ir
*Corresponding author

Abstract: In this paper, an extended topology for the design of a high voltage gain n-port bidirectional DC-DC converter with decreased voltage stress on the switches is developed. First, dual-port and three-port conventional converters are investigated; afterwards, the extended four and n-port bidirectional converters are analysed based on the concept of these basic models. Some advantages of the proposed topology are its simple configuration with a reduced number of switches and small size due to the use of no transformer in the topology. In the results, the voltage stress on switches, minimum and maximum current values of the inductors and the voltage gain between the lower voltage source and the upper one are calculated for the extended n-port converter. As a typical case, a four-port converter is designed and simulated by the PSCAD software and by controlling the duty cycle of the converter, which is extracted from an incremental conduction algorithm, the maximum power of the photovoltaic (PV) module is extracted in varying environmental conditions. In addition, to validate the operational performance of the four-port converter and evaluate the presented analysis, a prototype was fabricated and the experimental results were also presented.

Keywords: bidirectional DC-DC converter; photovoltaic module; maximum power point tracking; MPPT; multi-port DC-DC converter; non-isolated DC-DC converter.

Reference to this paper should be made as follows: Bahravar, S., Abbaszadeh, K. and Olamaei, J. (2022) 'A multi-port non-isolated bidirectional DC-DC converter', *Int. J. Power Electronics*, Vol. 15, No. 1, pp.86–115.

Biographical notes: Sepideh Bahravar received her BS in Electrical Engineering from the Department of Engineering, University of Shahroud, Shahroud, Iran, in 2007 and her MS from Islamic Azad University, Science and Research Branch Tabriz, Tabriz, Iran, in 2012, graduating with first class honours. Now, she is currently working toward her PhD degree in Electrical Engineering in the Department of Electrical and Computer Engineering, Islamic Azad University, South Tehran Branch, Tehran, Iran. She is the author of several journal and conference papers. Her current research interests include the analysis and control of power electronic converters and their applications.

Copyright © 2022 Inderscience Enterprises Ltd.

Karim Abbaszadeh received his BS degree in Communication Engineering from the K.N. Toosi University of Technology, Tehran, in 1991, and the MS and PhD degrees in Electrical Engineering from the Amir Kabir University of Technology, Tehran, Iran, in 1997 and 2000 respectively. From 2001 to 2003, he was a Research Assistant in the Electrical Engineering Department, Texas A&M University, College Station. He is currently an Associate Professor with the Electrical Engineering Department, K.N. Toosi University of Technology. His research interests include power electronic and DC-DC and DC-AC converter, electric machinery, variable-speed drives, and propulsion applications. He is the author of more than 50 published journal papers. He is actively involved in presenting short courses and consulting in his area of expertise to various industries.

Javad Olamaei received his BSc, MSc and PhD degrees in Power Engineering from the University of Tabriz, Amirkabir University of Technology and Islamic Azad University Science and Research Branch Tehran University respectively. Currently, he is an Associated Professor in the Department of Electrical Engineering, Islamic Azad University, South Tehran Branch, Tehran, Iran. His interests include power distribution system planning and impact of DGs on the power system.

1 Introduction

Nowadays due to the environmental pollution and lack of energy sources, renewable energy sources such as PV energy has gained a lot of attention (Forouzesh et al., 2018). One of the major issues in direct connection of PV modules to the consumption loads is the low efficiency of the PV system due to the variations in the output voltage and current of these modules (Nathan et al., 2018). Growing economies should build houses and buildings in the years to come. Since electricity is limited and expensive, the use of solar cells is very cost effective and attractive. The DC line has many benefits to homes, but the main question is that what is the effect of the radiation, temperature, and the output load on the output voltage and current variations in PV systems (Jalihal et al., 2018). Therefore, in order to increase the efficiency of PV modules, the generated electrical energy is supplied to the consumer through DC-DC converters. Under this circumstance, the maximum PV power is extracted by means of controlling the duty cycle of the converter. According to Esram and Chapman (2007), to control the duty cycle, among different methodologies introduced for 'maximum power extraction', the incremental conduction method with various step, effectively tracks the maximum power point in varying environmental conditions and due to small number of fluctuations about the maximum power point, the optimum speed for reaching the steady state response is better compared with the other methodologies. Noted that utilising multiple PV modules instead of using only one larger PV module is preferred to generate more power and increasing reliability of the PV system (Rahman, 2012). As a typical case, the maximum power point of a PV system is achieved through a three-port step-up converter (Wang and Li, 2013). Generally speaking, the selection and design of a converter with features such as high efficiency, low switching losses and small ripple in the output load voltage and current is of considerable significance.

Given that the bidirectional DC-DC converters can be regarded for utilisation in PV systems, three-port bidirectional DC-DC converters were presented in Wu and Chen (2019) and Katayama et al. (2016). In Katayama et al. (2016), a battery is employed to compensate the overload and underload. In doing that, the battery is charged during overload and discharged during underload. The power quantity can be controlled owing to the duty cycle control of the switches.

Hybrid systems require multiport converters to combine input energy sources with different voltage-current characteristics to produce the desired output voltage. These low-cost multiport converters have simple topologies, central controller, and high reliability (Farakhor et al., 2019; Mohseni et al., 2018). The multi-input multi-output (MIMO) converter in Mohseni et al. (2018) benefits from diode-capacitor voltage multiplier stages for each corresponding output port to increase the voltage levels of the outputs. However, it requires a number of inductors and diodes, which lead to enhancing the design complexity.

In recent years, several topologies have been introduced for multiport converters including multi-input single-output, single-input multi-output, and MIMO, which are suitable for variety of applications, including PV systems and hybrid electric machines (Babaei et al., 2017c; Immanuel et al., 2016; Rehman et al., 2015; Shahir et al., 2017; Khosrogorji et al., 2016). In Kardan et al. (2017), a high voltage gain DC/DC boost converter with three input ports is suggested to be used for hybrid PV/fuel cell /battery applications. In the multiport converter introduced in Kardan et al. (2017), several functionalities like tracking the maximum power of the PV source, setting the fuel cell power, controlling the battery power, and calibrating the output voltage are feasible thanks to the control of the duty ratios of the applied switches. Dhananjaya and Pattnaik (2019) developed a topology to implement a single-input multi-output DC-DC converter. In these configurations, the multiport outputs are feasible by controlling the current of inductors and adopting a proper duty cycle for switching devices. In this regard, in Dos Santos (2013), the modelling and controller design for a single input two-output, DC-DC buck converter with reduced circuit elements and bidirectional power flow is suggested which can be used in the application of electric motor drive systems. This topology offers high efficiency, lower power loss, and reduced number of switching devices. However, it requires high current switches, which leads to the higher costs. Another disadvantage of this topology is its low reliability as compared with voltage source converters. By the same token, Deihimi et al. (2017) have developed a bidirectional, high efficiency single-input triple-output, DC-DC converter with high voltage gain, which works based on soft-switching technique for high step-up applications.

In contrast to Dhananjaya and Pattnaik (2019), Dos Santos (2013) and Wai and Zhang (2019), Deihimi et al. (2017) have proposed a novel extendable multi-input single-output step-up DC-DC converter with enhanced voltage gain. Because of flexible output voltage level, which depends on the number of the input ports, the converter developed in Deihimi et al. (2017) is suitable for various hybrid energy systems.

In recent years, the MIMO converters are gaining popularity due to their ability to combine several input voltage sources and produce several voltage levels at their output terminals. There are various methods to design MIMO converters. One method is to connecting the multi-input converters in series with multi-output converters. In Behjati and Davoudi (2013), a MIMO DC-DC converter with arbitrary voltage gain level is proposed, which can manage arbitrary number of input sources and output loads. In this topology many switches are used. In other words, this converter requires as many

switches as its input-output terminals, which increases the complexity of the converter. For the higher number of input sources and output loads, the power sharing between the connected loads reduces. Moreover, the number of switches and input sources significantly increase as the number of output increases. In Babaei and Abbasi (2015), a novel topology for MIMO DC-DC boost converter is proper to use in applications like PV and fuel cell systems.

The analysis and design considerations of the soft-switching boost DC/DC converter presented in Babaei et al. (2017a) shows that the losses occurred in switching devices are decreased. Other advantages of the topology of Babaei et al. (2017a) are the reduction of the voltage and current stresses of the circuit components, due to soft-switching feature, and its high switching frequency. In Babaei et al. (2017b), a novel high step-up high step-down bidirectional DC-DC converter is introduced in which the voltage conversion ratio is increased by using two coupled inductors and switched capacitor circuit in both boost and buck operation modes. In Kunalkumar et al. (2019), an additional bi-directional buck-boost converter is proposed for energy storage. Kunalkumar et al. (2019) employed a dual switch forward snubber circuit as auxiliary circuits, which are needed in almost conventional isolated boost converters, along with dual active bridge (DAB) converter in the proposed converter. The proposed converter in Kunalkumar et al. (2019) has distinct advantages like zero voltage switching starting (ZVS), no voltage stress on main switches, no additional conduction losses and improved efficiency as compared to RCD snubber-based converter system. In this regard, recently, Jayasankar and Vinutha (2018) have presented a low-cost high-efficiency interleaved buck DC-DC converter using zero current switching (ZCS) resonant with additional inductor and capacitor. The main advantage of the converter introduced in Jayasankar and Vinutha (2018) is the behaviour of easy control under the ZCS condition, which leads to reducing the switching losses.

In light of description, it can be concluded that mathematical modelling of power electronic circuits like converters and inverters is one of the basic subjects in analysis of their operations, which always has been considered by the power electronic engineers and researchers (Bahravar et al., 2012a, 2012b; Babaei et al., 2015).

In this paper, an extendable topology for a high voltage gain n-port bidirectional DC-DC converter with decreased voltage stress on the switches is proposed. The advantage of the extendable topology is its simple configuration with reduced number of switches, capable of extending to any number of desirable ports, no need for passive equipment, and overall small size thanks to not to use transformer in the topology while keeping its operational performance. In addition, by controlling the duty cycle of the extended converter, which is extracted from a well-established incremental conduction algorithm, the maximum power point of PV system for various environmental conditions (various radiations), is achieved. The use of incremental conduction algorithm leads to provide acceptable response, i.e., track the peak power point accurately at different atmospheric conditions. In the results, the voltage stresses, maximum and minimum current in the inductors, and the voltage gain between the lower and upper voltage sources for this extendable topology are calculated analytically. Without loss of generality, a four-port converter based on the applied topology is developed and the maximum power of each PV module, which can be supplied to the output load, is realised through incremental conduction with variable step size maximum power point tracking (MPPT) algorithm. By increasing the number of input voltage sources, the MPPT simulation time increases. To validate the optimum performance of a PV system

including the linear equivalent circuit for PV, the introduced four-port bidirectional DC-DC converter along with output load and MPPT controller are simulated by the PSCAD software. The experimental results are provided to further support the simulation results and verify the presented analysis.

The organisation of this paper is as follows. Section 2 introduces the operation modes of a conventional dual-port bidirectional converter. Section 3 explains the working states of a three-port bidirectional converter, which comes from two-port converter concepts. The extended four-port bidirectional converter is discussed in Section 4. Sections 5 explains the working states of an extended n-port bidirectional converter. In Section 6, the approach based on the use of incremental conduction with variable step size MPPT algorithm is adopted for the realisation of maximum PV power. Simulation and experimental results are presented in Section 7. Finally, the conclusion is given in Section 8.

2 Conventional dual-port bidirectional converter

The power circuit for the conventional dual-port bidirectional converter is depicted in Figure 1, which is inspired from topology presented in Katayama et al. (2016). The switching pulses for this converter are illustrated in Figure 2. Regarding Figure 2, at each moment, only one switch is conducting. Figure 2 is demonstrated for the duty cycle equal to 1/2 so that both the switches conduct for 1/2 of the switching period and are off for 1/2 of the switching period. This converter has two operational modes in one period, which are the times interval $t_D \le t \le t_1$ and $t_1 \le t \le T_s$, for the first and second operational modes, respectively. The switches S_2 and S_1 turn off at the beginning time of the first and second modes, respectively. In this regard, the voltage stress across the corresponding off-switch is equal to be V_H. Therefore, the voltage v_{L1} is equal to $v_{l1} - V_H$ and for the first and second modes, respectively. Accordingly, the current of the switches S_1 and S_2 for the first and second modes are obtained as:

$$i_{S1} = i_{L1} = I_{m21} + \frac{V_{\ell 1}}{L_1}\left(t - t_0\right) \tag{1}$$

$$-i_{S2} = i_{L1} = I_{m11} + \frac{V_{\ell 1} - V_H}{L_1}\left(t - t_0\right) \tag{2}$$

Figure 1 Power circuit of the conventional dual-port bidirectional converter

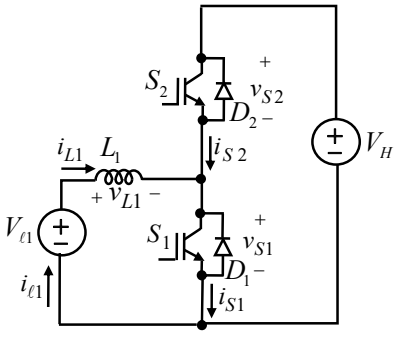

Figure 2 Triggering pulses for the switches of the conventional dual-port bidirectional converter (see online version for colours)

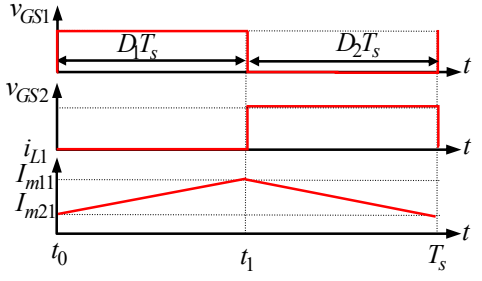

2.1 Voltage gain calculation

In steady state, according to the voltage balance law for the inductor existing in the circuit of Figure 1, the average voltage v_{L1} is equal to zero which is expressed in the following:

$$D_1T_sV_{\ell 1} + D_2T_s\left(V_{\ell 1} - V_H\right) = 0 \tag{3}$$

By simplifying the equation (3), the transfer ratio for the lower and upper voltage sources is derived as:

$$\frac{V_H}{V_{\ell 1}} = \frac{1}{D_2} \tag{4}$$

2.2 Maximum and minimum current of the inductor

The average value of the current i_{L1} is equal to the average value of the current i_{l1}. In other words, in one switching period of T_s it can be written that:

$$I_{\ell 1} = \frac{I_{m11} + I_{m21}}{2} \tag{5}$$

By rewriting the equation (1) at the time t_1, the equation (6) is achieved for the step-up operation:

$$I_{m11} = I_{m21} + \frac{V_{\ell 1}}{L_{mj}}D_1T_s \tag{6}$$

By substituting the current value I_{m11} from the relation (5) in the relation (6), it can be written the following relations as:

$$I_{m21} = I_{\ell 1} - \frac{V_{\ell 1}}{2L_1}D_1T_s \tag{7}$$

$$I_{m11} = I_{\ell 1} + \frac{V_{\ell 1}}{2L_1}D_1T_s \tag{8}$$

3 Three-port bidirectional converter

The power circuit for three-port bidirectional converter is depicted in Figure 3. The switching pulses for the presented three-port converter is shown in Figure 4. With regards to Figure 4 at each moment only two switches are conducting. Figure 4 is illustrated for duty cycle of 2/3, in a way that for 2/3 of the switching period, all three switches are *on* and for 1/3 of the switching period, they are off. The duty cycle D for each switch is $D = D_1 + D_2$. There are three operational modes within a switching period of this converter, which are studied in the following.

Figure 3 Power circuit for the three-port bidirectional DC-DC converter

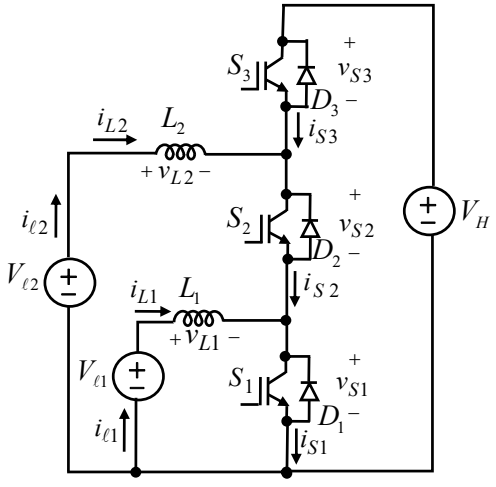

Figure 4 Triggering pulses for switches three-port bidirectional converter (see online version for colours)

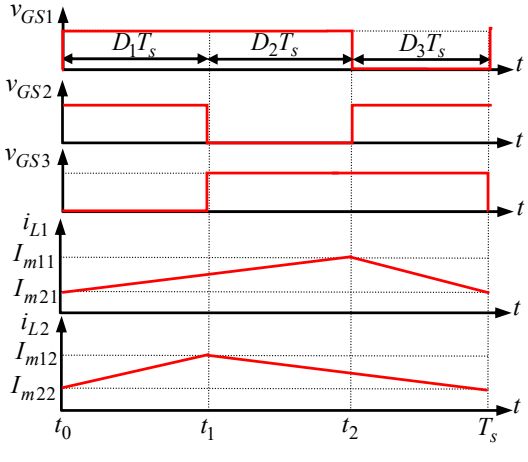

3.1 First operational mode (time interval $t_0 \le t \le t_1$)

According to Figure 4, at the time t_0 the switch S_3 turns off. The voltage stress across the switch S_3, that is v_{S3}, is equal to V_H in this operational mode. During this mode of operation voltages v_{L1} and v_{L2} are equal to V_{l1} and V_{l2}, respectively. Therefore, the current in the inductors and the switches are calculated as follows:

$$i_{L1} = I_{m21} + \frac{V_{\ell 1}}{L_1}\left(t - t_0\right) \tag{9}$$

$$i_{S2} = i_{L2} = I_{m22} + \frac{V_{\ell 2}}{L_2}\left(t - t_0\right) \tag{10}$$

$$i_{S1} = i_{L1} + i_{L2} = I_{m21} + I_{m22} + \left(\frac{V_{\ell 1}}{L_1} + \frac{V_{\ell 2}}{L_2}\right)\left(t - t_0\right) \tag{11}$$

In above equations I_{m21}, I_{m22} are the initial current values for iL_1 and iL_2.

3.2 Second operational mode (time interval $t_1 \le t \le t_2$)

According to Figure 4 at the beginning of this mode, the switch S_2 turns off. The voltage stress across this switch, *i.e.*, v_{S2}, in this mode of operation is V_H. During this mode, the voltages v_{L1} and v_{L2} are equal to V_{l1} and $V_{l2} - V_H$, respectively. Thus, according to the relation (9) the current in the inductors and the switches are calculated as follows:

$$-i_{S3} = i_{L2} = I_{m12} + \frac{V_{\ell 2} - V_H}{L_2}\left(t - t_1\right) \tag{12}$$

$$i_{S1} = i_{L1} = I_{m21} + \frac{V_{\ell 1}}{L_1}\left(t - t_0\right) \tag{13}$$

In equation (12), I_{m12} is the initial value for the current i_{L2} at the beginning of this operational mode.

3.3 Third operational mode (time interval $t_2 \le t \le T_s$)

According to Figure 4, at the time t_2 the switch S_1 turns off. The voltage stress across the switch, that is v_{s1}, is V_H in this mode of operation. During this mode, the voltages v_{L1} and v_{L2} are equal to $V_{l1} - V_H$ and $V_{l2} - V_H$, respectively. Therefore, from equation (12) the current in the inductors and the switches are achieved as follows:

$$-i_{S2} = i_{L1} = I_{m11} + \frac{V_{\ell 1} - V_H}{L_1}\left(t - t_2\right) \tag{14}$$

$$i_{S3} = -\left(i_{L2} + i_{L1}\right) = -\left[I_{m12} + \frac{V_{\ell 2} - V_H}{L_2}\left(t - t_1\right) + I_{m11} + \frac{V_{\ell 1} - V_H}{L_1}\left(t - t_2\right)\right] \tag{15}$$

In equation (15), I_{m11} is the initial value of the current i_{L1} at the beginning of this operational mode. The voltage calculation as well as the maximum and minimum currents of the applied inductor are calculated in the next subsection.

3.4 Voltage gain calculation

In steady state, according to the voltage balance law for the inductor existing in the circuit shown in Figure 3, the average voltages v_{L1} and v_{L2} is equal to zero. Therefore, the voltage balance relation for the inductor L_1 is given as:

$$\left((D_1 + D_2)T_s V_{\ell 1} + D_3 T_s \left(V_{\ell 1} - V_H\right) = 0 \right. \tag{16}$$

The voltage balance relation for the inductor L_2 is given as:

$$D_1 T_s V_{\ell 2} + \left(D_3 + D_2\right) T_s \left(V_{\ell 2} - V_H\right) = 0 \tag{17}$$

By simplifying the relations (16) and (17), the transfer ratio for the lower and upper voltage sources is derived as:

$$\frac{V_H}{V_{\ell 1}} = \frac{1}{D_3} = \frac{2}{D} \tag{18}$$

$$\frac{V_H}{V_{\ell 2}} = \frac{1}{D_2 + D_3} = \frac{1}{D} \tag{19}$$

To exploit three different voltage levels that are specified in prior, according to the relations (18) and (19), the values of duty cycles should be attained as below:

$$D_1 = \frac{V_H - V_{\ell 2}}{V_H} \tag{20}$$

$$D_2 = \frac{V_{\ell 2} - V_{\ell 1}}{V_H} \tag{21}$$

$$D_3 = \frac{V_{\ell 1}}{V_H} \tag{22}$$

4 Extended four-port bidirectional converter

The power circuit of the extended four-port bidirectional converter is depicted in Figure 5. It is worth noting that each DC voltage source in the extended converter can have step-down operation (exploited as resistive load) or step-up operation (exploited as input voltage source). The switching pulses for the extended four-port converter are shown in Figure 6. The inductances L_1, L_2, L_3, and L_4 are utilised for storing and transferring energy in both directions in every stage. Duty cycle D for each switch is equal to $D = D_1 + D_2 + D_3$. There are four modes of operation in the extended converter, which are described in the following.

Figure 5 Power circuit of the extended four-port bidirectional DC-DC converter

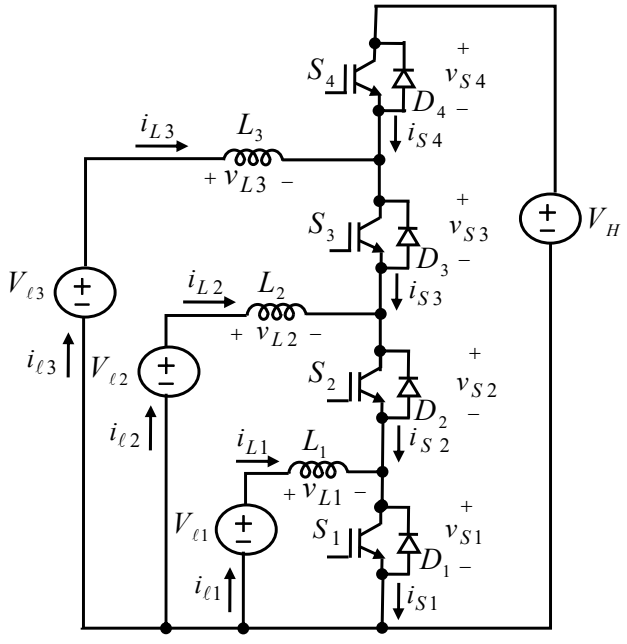

Figure 6 Waveforms for the extended four-port bidirectional DC-DC converter (see online version for colours)

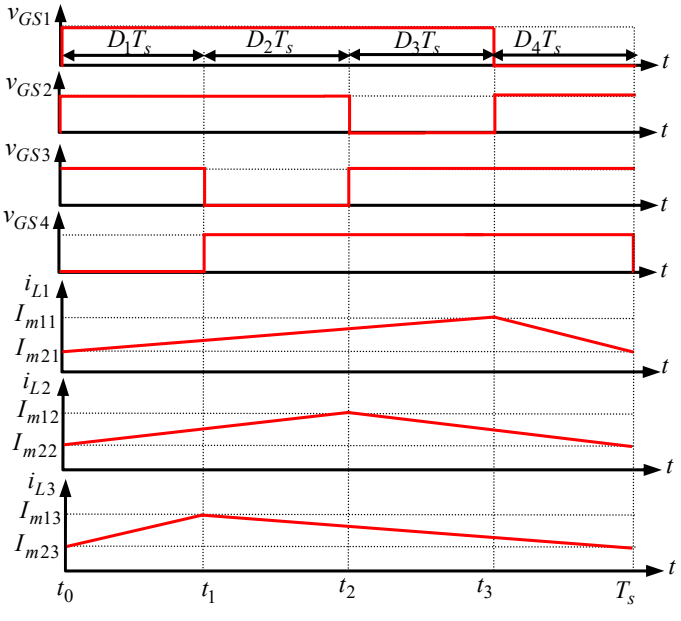

4.1 First mode of operation (time interval $t_0 \le t \le t_1$)

According to Figure 6, at the time t_0 the switch S_4 turns off. The voltage stress across the switch S_4, i.e., v_{s4}, is V_H in this mode of operation. During this mode, the voltages v_{L1}, v_{L2}, and v_{L3} are equal to V_{l1}, V_{l2}, and V_{l3}, respectively. Therefore, the current in the inductors and the switches are obtained as follows:

$$i_{L1} = I_{m21} + \frac{V_{\ell 1}}{L_1}\left(t - t_0\right) \tag{23}$$

$$i_{L2} = I_{m22} + \frac{V_{\ell 2}}{L_2}\left(t - t_0\right) \tag{24}$$

$$i_{S3} = i_{L3} = I_{m23} + \frac{V_{\ell 3}}{L_3}\left(t - t_0\right) \tag{25}$$

$$i_{S2} = i_{L2} + i_{L3} = I_{m23} + I_{m22} + \left(\frac{V_{\ell 3}}{L_3} + \frac{V_{\ell 2}}{L_2}\right)\left(t - t_0\right) \tag{26}$$

$$i_{S1} = i_{L1} + i_{L2} + i_{L3} = I_{m21} + I_{m23} + I_{m22} + \left(\frac{V_{\ell 1}}{L_1} + \frac{V_{\ell 3}}{L_3} + \frac{V_{\ell 2}}{L_2}\right)\left(t - t_0\right) \tag{27}$$

In above relations I_{m21}, I_{m22}, and I_{m23} are the initial value for the currents i_{L1}, i_{L2}, and i_{L3}, respectively.

4.2 Second mode of operation: time interval $t_1 \le t \le t_2$

According to Figure 6, at the beginning of this mode of operation, the switch S_3 turns off. The voltage stress across the switch S_3, i.e.,v_{S3}, is V_H in this mode of operation. During this mode, the voltages v_{L1}, v_{L2} and v_{L3} are equal to V_{l1}, V_{l2}, and $V_{l3} - V_H$, respectively. Therefore, based on the relations (23) and (24) the current in the inductors and the switches are calculated as follows:

$$-i_{S4} = i_{L3} = I_{m13} + \frac{V_{\ell 3} - V_H}{L_3}\left(t - t_1\right) \tag{28}$$

$$i_{S2} = i_{L2} = I_{m22} + \frac{V_{\ell 2}}{L_2}\left(t - t_0\right) \tag{29}$$

$$i_{S1} = i_{L1} + i_{L2} = I_{m21} + I_{m22} + \left(\frac{V_{\ell 1}}{L_1} + \frac{V_{\ell 2}}{L_2}\right)\left(t - t_0\right) \tag{30}$$

In relation (28), I_{m13} is the initial value for current i_{L3} at the beginning of this operational mode.

4.3 Third mode of operation (time interval $t_2 \le t \le t_3$)

According to Figure 6, at the time $t_2$the switch S_2 turns off. The voltage stress across the switch S_2, i.e., v_{S2}, is V_H in this mode of operation. During this mode, the voltages v_{L1}, v_{L2} and v_{L3} are equal to V_{l1}, $V_{l2} - V_H$, and $V_{l3} - V_H$, respectively. Therefore, based on the relation (23), the current in the inductors and the switches are obtained as follows:

$$-i_{S3} = i_{L2} = I_{m12} + \frac{V_{\ell 2} - V_H}{L_2}\left(t - t_2\right) \tag{31}$$

$$i_{S1} = i_{L1} = I_{m21} + \frac{V_{\ell 1}}{L_1}\left(t - t_0\right) \tag{32}$$

$$\begin{aligned} i_{S4} &= -\left(i_{L2} + i_{L3}\right) = \\ &-\left[I_{m13} + I_{m12} + \frac{V_{\ell 3} - V_H}{L_3}\left(t - t_1\right) + \frac{V_{\ell 2} - V_H}{L_2}\left(t - t_2\right)\right] \end{aligned} \tag{33}$$

In equation (31), I_{m12} is the initial value for current i_{L2} at the beginning of this operational mode.

4.4 Fourth mode of operation (time interval $t_3 \le t \le T_s$)

According to Figure 6, at the time t_3 the switch S_1 turns off. The voltage stress across the switch S_1, *i.e.*, v_{S1}, is V_H in this mode of operation. During this mode, the voltages v_{L1}, v_{L2} and v_{L3} are equal to $V_{l1} - V_H$, $V_{l2} - V_H$ and $V_{l3} - V_H$, respectively. Therefore, the current in the inductors and the switches are achieved as follows:

$$i_{S2} = -i_{L1} = -\left[I_{m11} + \frac{V_{\ell 1} - V_H}{L_1}\left(t - t_3\right)\right] \tag{34}$$

$$i_{S3} = -\left(i_{L1} + i_{L2}\right) = -\left[I_{m11} + I_{m12} + \frac{V_{\ell 1} - V_H}{L_1}\left(t - t_3\right) + \frac{V_{\ell 2} - V_H}{L_2}\left(t - t_2\right)\right] \tag{35}$$

$$\begin{aligned} i_{S4} = -\left(i_{L1} + i_{L2} + i_{L3}\right) = -\Bigg[& I_{m11} + I_{m12} + I_{m13} + \frac{V_{\ell 1} - V_H}{L_1}\left(t - t_3\right) \\ & + \frac{V_{\ell 2} - V_H}{L_2}\left(t - t_2\right) + \frac{V_{\ell 3} - V_H}{L_3}\left(t - t_1\right)\Bigg] \end{aligned} \tag{36}$$

In relation (34) I_{m11} is the initial value of the current i_{L1} at the beginning of this operational mode.

4.5 Voltage gain calculation

In steady state, according to the voltage balance law for the three inductors existing in the circuit in Figure 5, the average voltages v_{L1}, v_{L2} and v_{L3} are equal to zero. Therefore, the voltage balance relation for the inductor L_1 is found as follows:

$$\left(D_1 + D_2 + D_3\right)T_s V_{\ell 1} + D_4 T_s \left(V_{\ell 1} - V_H\right) = 0 \tag{37}$$

Also, the voltage balance relation for the inductor L_2 is written as follows:

$$\left(D_1 + D_2\right)T_s V_{\ell 2} + (D_3 + D_4)T_s \left(V_{\ell 2} - V_H\right) = 0 \tag{38}$$

The voltage balance relation for the inductor L_3 is written as follows:

$$D_1 T_s V_{\ell 3} + \left(D_2 + D_3 + D_4\right)T_s \left(V_{\ell 3} - V_H\right) = 0 \tag{39}$$

By simplifying the relations (37) to (39), the transfer ratio for the lower and upper voltage sources is derived as:

$$\frac{V_H}{V_{\ell 1}} = \frac{1}{D_4} = \frac{3}{D} \tag{40}$$

$$\frac{V_H}{V_{\ell 2}} = \frac{1}{D_4 + D_3} = \frac{3}{2D} \tag{41}$$

$$\frac{V_H}{V_{\ell 3}} = \frac{1}{D_4 + D_3 + D_2} = \frac{1}{D} \tag{42}$$

4.6 Maximum and minimum currents of the inductors

The average value of the currents i_{L1}, i_{L2}, and $i_{L3}$is equal to the average value of currents i_{l1}, i_{l2}, and i_{l3}. In other words, during one switching period T_s it can be written:

$$I_{\ell 1} = \frac{I_{m11} + I_{m21}}{2} \tag{43}$$

By rewriting the relation (23) at the time t_3, the relations in the following is obtained for the step-up operation:

$$I_{m11} = I_{m21} + \frac{V_{\ell 1}}{L_1}\left(D_1 + D_2 + D_3\right)T_s \tag{44}$$

Substituting the value of current I_{m11} from the relation (43) in relation (44) it can be written that:

$$I_{m21} = I_{\ell 1} - \frac{V_{\ell 1}}{2L_1}\left(D_1 + D_2 + D_3\right)T_s \tag{45}$$

$$I_{m11} = I_{\ell 1} + \frac{V_{\ell 1}}{2L_1}\left(D_1 + D_2 + D_3\right)T_s \tag{46}$$

By rewriting the relation (24) at time t_2, the relation (47) is achieved for the step-up operation:

$$I_{m12} = I_{m22} + \frac{V_{\ell 2}}{L_2}(D_1 + D_2)T_s \tag{47}$$

Similar to the earlier mentioned state, the maximum and minimum values for the current of inductor L_2 is achieved as follows:

$$I_{m22} = I_{\ell 2} - \frac{V_{\ell 2}}{2L_2}(D_1 + D_2)T_s \tag{48}$$

$$I_{m12} = I_{\ell 2} + \frac{V_{\ell 2}}{2L_2}(D_1 + D_2)T_s \tag{49}$$

Similar to the two earlier mentioned states, the maximum and minimum values for the current of inductor L_3 is obtained as follows:

$$I_{m23} = I_{\ell 3} - \frac{V_{\ell 3}}{2L_3}D_1T_s \tag{50}$$

$$I_{m13} = I_{\ell 3} + \frac{V_{\ell 3}}{2L_3}D_1T_s \tag{51}$$

All the relations above are true for the step-down operation, only the direction of the currents I_{l1}, I_{l2} and I_{l3} changes.

5 Extended n-port bidirectional converter

The power circuit of the extended *n*-port bidirectional converter is illustrated in Figure 7. This converter is operable if the relation $V_{l1} \le V_{l2} \le V_{l(N-1)} \le V_H$ holds for the DC voltage sources. Each stage in the extended converter can have step-down operation (exploited as a resistive load) or step-up operation (exploited as an input voltage source). Switching pulses for the extended *n*-port converter is illustrated in Figure 8. The inductances L_1, L_2, L_{n-1} are used in each stage for storing and transferring the energy. According to Figure 7, the extended *n*-port converter consists of n switches. Based on Figure 8, in one period of T_s, $n-1$ of these switches are in conduction mode. Assuming that D_1, D_2, D_1 ,…, D_{n-1}, D_n have equal values, accordingly the value of each D_n is equal to $1/n$. The duty cycle value for one switch is $(n-1)D_1$. In other words, it can be written as:

$$D = (n-1)D_1 = \frac{n-1}{n} \tag{52}$$

All the switches have the same phase shift for the triggering moment equal to $360/n$ degrees or $2\pi/n$ radians. The voltage stress for all the switches in the extended converter is as V_H. In a switching period, the extended converter has *n* modes of operation, which are given in the following.

Figure 7 Power circuit of the extended *n*-port bidirectional DC-DC converter

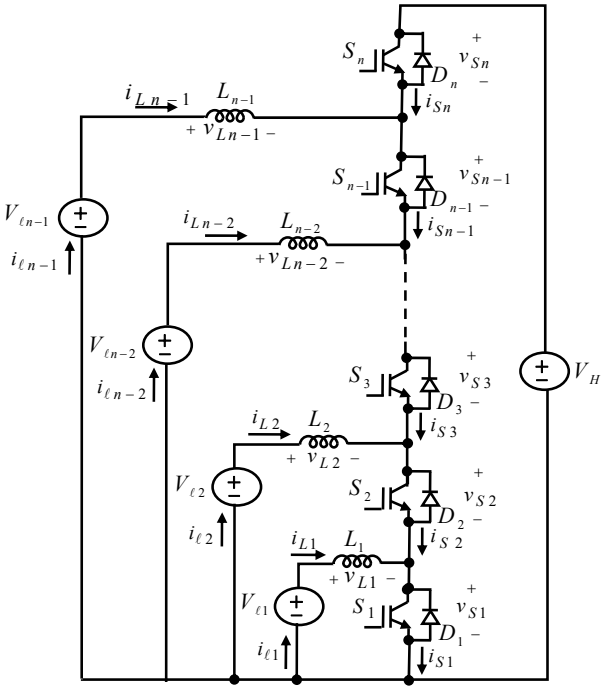

Figure 8 Switching pulses for the extended *n*-port bidirectional DC-DC converter (see online version for colours)

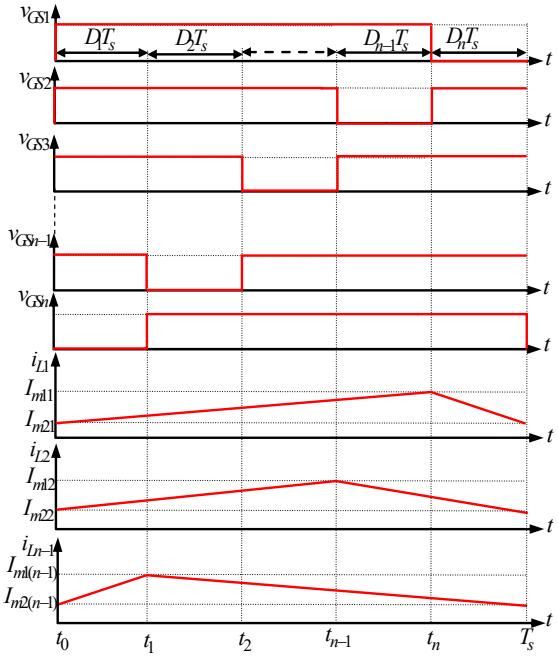

5.1 First mode of operation (time interval $t_0 \le t \le t_1$)

As can be observed from Figure 8, at the time t_0 the switch S_n turns off. The voltage stress across the switch S_n *i.e.*, v_{Sn} is equal to V_H. The voltages v_{L1}, v_{L2}, …, v_{Ln-1} are equal to V_{l1}, V_{l2},…, V_{ln-1}, respectively. Therefore, the current of the inductors and the switches can be obtained as follows:

$$i_{L1} = I_{m21} + \frac{V_{\ell 1}}{L_1}\left(t - t_0\right) \tag{53}$$

$$i_{L2} = I_{m22} + \frac{V_{\ell 2}}{L_2}\left(t - t_0\right) \tag{54}$$

$$i_{Sn-1} = i_{Ln-1} = I_{m2(n-1)} + \frac{V_{\ell n-1}}{L_{n-1}}\left(t - t_0\right) \tag{55}$$

$$\begin{aligned} i_{S(n-2)} &= i_{Sn-1} + i_{Ln-2} = I_{m2(n-1)} + \frac{V_{\ell n-1}}{L_{n-1}}\left(t - t_0\right) \\ &\quad + I_{m2(n-2)} + \frac{V_{\ell n-2}}{L_{n-2}}\left(t - t_0\right) \end{aligned} \tag{56}$$

$$\begin{aligned} &i_{S1} = i_{Ln-1} + i_{Ln-2} + \cdots + i_{L1} = I_{m2(n-1)} + I_{m2(n-2)} + \cdots + I_{m21} \\ &+ \left(\frac{V_{\ell n-1}}{L_{n-1}} + \frac{V_{\ell n-2}}{L_{n-2}} + \cdots \frac{V_{\ell 1}}{L_1} \right)\left(t - t_0\right) \end{aligned} \tag{57}$$

In above relations I_{m21}, I_{m22}, $I_{m2(n-1)}$, $I_{m2(n-2)}$ are the initial value for the currents i_{L1}, i_{L2}, i_{Ln-1}, i_{Ln-2}.

5.2 Second mode of operation: time interval $t_1 \le t \le t_2$

As can be seen from Figure 8, the switch S_{n-1} turns off at the beginning of this mode of operation. The voltage stress across the switch S_{n-1}, *i.e.*, v_{Sn-1}, is equal to V_H. During this mode of operation the voltages v_{L1}, v_{L2}, …, v_{Ln-2} are equal to V_{l1}, V_{l2},…, V_{ln-2}, respectively. The voltage V_{ln-1} is equal to $V_{ln-1} - V_H$. Therefore, according to the relations (53), (54) the current of the inductors and the switches can be obtained as follows:

$$-i_{Sn} = i_{Ln-1} = I_{m1(n-1)} + \frac{V_{\ell n-1} - V_H}{L_{n-1}}\left(t - t_1\right) \tag{58}$$

$$i_{Sn-2} = i_{Ln-2} = I_{m2(n-2)} + \frac{V_{\ell(n-2)}}{L_{n-2}}\left(t - t_0\right) \tag{59}$$

$$i_{S1} = i_{Ln-2} + \cdots + i_{L1} = I_{m2(n-2)} + \cdots + I_{m21} + \left(\frac{V_{\ell n-2}}{L_{n-2}} + \cdots \frac{V_{\ell 1}}{L_1} \right)\left(t - t_0\right) \tag{60}$$

In the relation (58) $I_{m1(n-1)}$ is the initial value for the current i_{Ln-1} at the beginning of this operational mode.

5.3 *(N – 1)th mode of operation (time interval $t_{n-1} \le t \le t_n$)*

As can be observed from Figure 8, at the time t_{n-1}, the switch S_2 turns off. The voltage stress across the switch S_2, *i.e.*, v_{S2} is equal to V_H. During this mode of operation the voltages v_{L1}, v_{L2},…, v_{Ln-1} are equal to V_{l1}, $V_{l2} - V_H$,…, $V_{ln-1} - V_H$, respectively. Therefore, according to the relations (53) the current of the inductors and the switches can be obtained as in the following:

$$i_{L2} = I_{m12} + \frac{V_{\ell 2} - V_H}{L_2}\left(t - t_{n-1}\right) \tag{61}$$

$$i_{S1} = i_{L1} = I_{m21} + \frac{V_{\ell 1}}{L_1}\left(t - t_0\right) \tag{62}$$

$$\begin{aligned} i_{Sn} &= -\left(i_{L2} + \cdots + i_{Ln-1}\right) = -\left[\left(I_{m12} + \cdots + I_{m1(n-1)}\right)\right. \\ &\left. + \left(\frac{V_{\ell 2} - V_H}{L_2}\left(t - t_{n-1}\right) + \cdots + \frac{V_{\ell n-1} - V_H}{L_{n-1}}\left(t - t_1\right)\right)\right] \end{aligned} \tag{63}$$

In the relation (61), I_{m12} is the initial value for the current i_{L2} at the beginning of this operational mode.

5.4 *N-th mode of operation (time interval $t_n \le t \le T_s$)*

According to Figure 8, at the time t_n the switch S_1 turns off. The voltage stress across the switch S_1, i.e., v_{S1} is equal to V_H. During this mode of operation the voltages v_{L1}, v_{L2}, …, v_{Ln-1} are equal to $V_{l1} - V_H$, $V_{l2} - V_H$,…, $V_{ln-1} - V_H$, respectively. Thus, the current of the inductors and the switches can be obtained as follows:

$$i_{S2} = -i_{L1} = -\left[I_{m11} + \frac{V_{\ell 1} - V_H}{L_1}\left(t - t_n\right)\right] \tag{64}$$

$$i_{S3} = -\left(i_{L1} + i_{L2}\right) = -\left[I_{m11} + I_{m12} + \frac{V_{\ell 1} - V_H}{L_1}\left(t - t_n\right) + \frac{V_{\ell 2} - V_H}{L_2}\left(t - t_{n-1}\right)\right] \tag{65}$$

$$\begin{aligned} i_{Sn} &= -\left(i_{L1} + i_{L2} + \cdots + i_{Ln-1}\right) = -\left(I_{m11} + I_{m12} + \cdots + I_{m1(n-1)}\right. \\ &\left. - \frac{V_{\ell 1} - V_H}{L_1}\left(t - t_n\right) + \frac{V_{\ell 2} - V_H}{L_2}\left(t - t_{n-1}\right) + \cdots + \frac{V_{\ell n-1} - V_H}{L_{n-1}}\left(t - t_1\right)\right) \end{aligned} \tag{66}$$

In the relation (64), I_{m11} is the initial value for the current i_{L1} at the beginning of this operational mode.

5.5 *Voltage gain calculation*

In steady state, according to the voltage balance law for the three inductors existing in the circuit in Figure 7, the average voltages v_{L1}, v_{L2}, …, and v_{Ln-1} are equal to zero. Based on Figure 8, the voltage balance relation for the inductor L_1 is written as in the following:

$$\left(D_1 + D_2 + D_3 + \cdots + D_{n-1}\right)T_s V_{\ell 1} + D_n T_s \left(V_{\ell 1} - V_H\right) = 0 \tag{67}$$

The voltage balance relation for the inductor L_2 is written as follows:

$$\left(D_1 + D_2 + \cdots + D_{n-2}\right)T_s V_{\ell 2} + \left(D_{n-1} + D_n\right)T_s \left(V_{\ell 2} - V_H\right) = 0 \tag{68}$$

The voltage balance relation for the inductor L_{n-2} is written as follows:

$$\left(D_1 + D_2\right)T_s V_{\ell n-2} + \left(D_3 + D_4 + \cdots D_{n-1} + D_n\right)T_s \left(V_{\ell n-2} - V_H\right) = 0 \tag{69}$$

The voltage balance relation for the inductor L_{n-1} is written as follows:

$$D_1 T_s V_{\ell n-1} + \left(D_2 + D_3 + D_4 + \cdots D_{n-1} + D_n\right)T_s \left(V_{\ell n-1} - V_H\right) = 0 \tag{70}$$

By simplifying the relations (67) to (70), the transfer ratio for the lower and upper voltage sources is derived as:

$$\frac{V_H}{V_{\ell 1}} = \frac{1}{D_n} = \frac{n-1}{D} \tag{71}$$

$$\frac{V_H}{V_{\ell 2}} = \frac{1}{D_{n-1} + D_n} = \frac{n-1}{2D} \tag{72}$$

$$\frac{V_H}{V_{\ell n-2}} = \frac{1}{D_3 + D_4 + \cdots D_{n-1} + D_n} = \frac{n-1}{(n-2)D} \tag{73}$$

$$\frac{V_H}{V_{\ell n-1}} = \frac{1}{D_2 + D_3 + D_4 + \cdots D_{n-1} + D_n} = \frac{n-1}{(n-1)D} = \frac{1}{D} \tag{74}$$

With regards to the relations (71) to (74), the transfer ratio relation for the lower and upper voltage sources in the extended n-port converter can be simplified as follows:

$$\frac{V_H}{V_{\ell K}} = \frac{n-1}{kD} \qquad k = 1, 2, 3, \ldots, n-2, n-1 \tag{75}$$

In the above relation, the parameter k is the number of the lower DC voltage source at the left side of the circuit of Figure 7. There are $n - 1$ DC voltage sources in the extended n-port converter. Substituting the value of D as a function of n from the relation (52) in the relation (75), the relation for the lower and the upper voltage source in the extended n-port can be obtained as follows:

$$\frac{V_H}{V_{\ell k}} = \frac{n}{k} \qquad k = 1, 2, 3, \ldots, n-2, n-1 \tag{76}$$

5.6 Maximum and minimum currents of the inductors

The average value of the currents i_{L1}, i_{L2}, …, and i_{Ln-1} are correspond to the average value of currents i_{l1}, i_{l2}, …, and i_{ln-1}. In other words, during one switching period T_s it can be written that:

$$I_{\ell 1} = \frac{I_{m11} + I_{m21}}{2} \tag{77}$$

By writing the relation (53) at the time t_n, the relation (78) is obtained for the step-up operation as:

$$I_{m11} = I_{m21} + \frac{V_{\ell 1}}{L_1} DT_s \tag{78}$$

Substituting the value of the current I_{m11} from the relation (77) in relation (75), the relation (79) and (80) will be obtained.

$$I_{m21} = I_{\ell 1} - \frac{V_{\ell 1}}{2L_1} DT_s = I_{\ell 1} - \frac{V_{\ell 1}}{2L_1}\left(\frac{n-1}{n}\right)T_s \tag{79}$$

$$I_{m11} = I_{\ell 1} + \frac{V_{\ell 1}}{2L_1} DT_s = I_{\ell 1} + \frac{V_{\ell 1}}{2L_1}\left(\frac{n-1}{n}\right)T_s \tag{80}$$

Writing the relation (54) at time t_{n-1}, the relation (81) is derived for the step-up operation:

$$I_{m12} = I_{m22} + \frac{V_{\ell 2}}{L_2}\left(\frac{n-2}{n}\right)T_s \tag{81}$$

Similar to the earlier mentioned state, the maximum and minimum values for the current of inductor L_2 is achieved as follows:

$$I_{m22} = I_{\ell 2} - \frac{V_{\ell 2}}{2L_2}\left(\frac{n-2}{n}\right)T_s \tag{82}$$

$$I_{m12} = I_{\ell 2} + \frac{V_{\ell 2}}{2L_2}\left(\frac{n-2}{n}\right)T_s \tag{83}$$

In addition, the maximum and minimum values for the current of inductor L_{n-1} are obtained as follows:

$$I_{m2(n-1)} = I_{\ell n-1} - \frac{V_{\ell n-1}}{2L_{n-1}}(1-D)T_s = I_{\ell n-1} - \frac{V_{\ell n-1}}{2L_{n-1}}\left(\frac{1}{n}\right)T_s \tag{84}$$

$$I_{m1(n-1)} = I_{\ell n-1} + \frac{V_{\ell n-1}}{2L_{n-1}}(1-D)T_s = I_{\ell n-1} + \frac{V_{\ell n-1}}{2L_{n-1}}\left(\frac{1}{n}\right)T_s \tag{85}$$

Considering the relations (77) to (85), the relations for the maximum and the minimum current of the switches as a function of the average current flowing through each stage can be simplified as follows:

$$I_{m2k} = I_{\ell k} - \frac{V_{\ell k}}{2L_k}\left(\frac{n-k}{n}\right)T_s \qquad k = 1,2,3,\ldots,n-2,n-1 \tag{86}$$

$$I_{m1k} = I_{\ell k} + \frac{V_{\ell k}}{2L_k}\left(\frac{n-k}{n}\right)T_s \qquad k = 1,2,3,\ldots,n-2,n-1 \tag{87}$$

As mentioned earlier, k is the number of the lower DC voltage source at the left side of the circuit of Figure 7. All of the above mentioned relations hold for the step-down operation, only the direction of the currents I_{l1}, I_{l2},…, I_{lk} changes.

6 Maximum power point tracking

The general structure of a PV system for simulation purposes is in accordance with Figure 9. The structure consists of an input PV source, an intermediary stage composed of a DC-DC converter, a MPPT control stage, and finally an output load. The characteristics of the utilised silicon module is provided in Table 1 which is extracted from Jalihal et al. (2018). For this type silicon module, the power-voltage (P-V) characteristic curves for various radiations are achieved as shown in Figure 10. These characteristic curves support the data provided by the manufacturers (presented in Table 1) under standard conditions. Regarding the fact that any change in radiation has more impact on the MPPT point compared with the change occurred in the temperature parameter; thus, in this part, the temperature of the cell is kept constant and the tracking of the MPPT point is analysed just for the case of various radiation conditions. Here, the significant and qualitative indices such as the constant voltage and the efficiency of the PV system are two determinative parameters, which accurately express the capability of the designed MPPT. In this work, the well-known incremental conduction MPPT algorithm with a variable step size is employed to control the duty cycle of DC-DC converter. It is worthwhile to note that during the simulation of the MPPT, the 'sampling frequency' is the influential parameter for proper extraction of the maximum power. This parameter should be considerably smaller than the 'switching frequency' of the converter.

Figure 9 General structure of a PV system

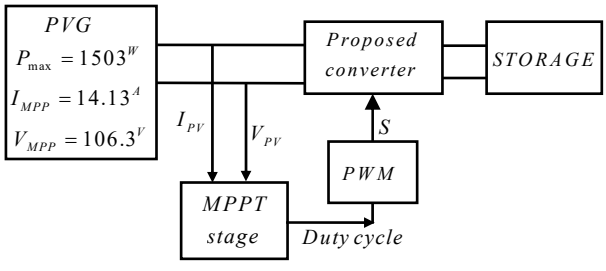

Figure 10 Characteristic curves of (a) P-V (b) I-V for the PV source under radiations 200 w/m^2, 400 w/m^2, 600 w/m^2, 800 w/m^2, and 100 w/m^2 (see online version for colours)

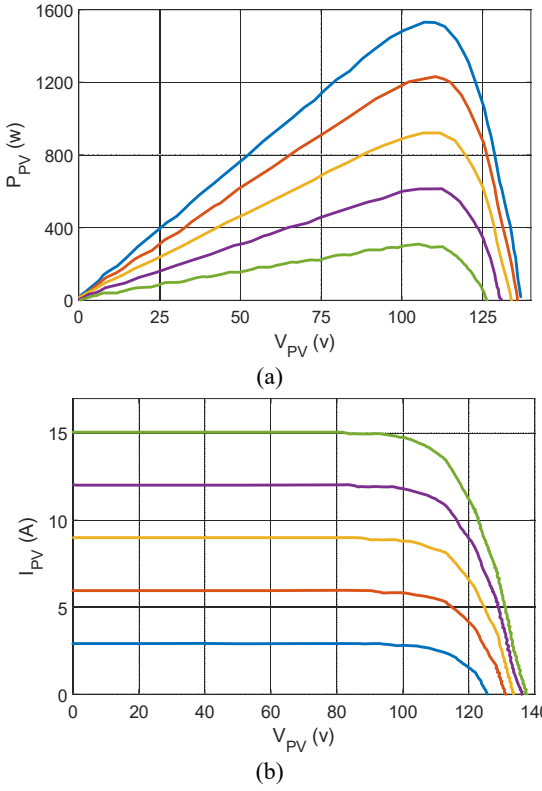

Table 1 Mono crystalline silicon module parameters provided in Jalihal et al. (2018) for the standard environmental conditions

Parameters	P_{max}	I_{sc}	V_{oc}	V_{MPP}	I_{MPP}	N_s
LPV85	85w	5.02A	22.9V	18.3V	4.64A	36

By controlling the duty cycle of the extended DC-DC converter, the maximum power can be extracted from the PV system in such a way that it guarantees the steady state operation of the PV system at the maximum power point. Here, D is the duty cycle of the converter which is used as the control signal for the incremental conduction algorithm with varying step.

The flowchart of the utilised incremental conduction algorithm with varying step to extract the MPPT is illustrated in Figure 11. In step-up operation, after sampling the voltage and the power of the PV and determining that the operating point is in the right side of the power-voltage characteristic curve shown in Figure 10, the proper command to the MPPT controller should be applied to decrease the PV voltage or increase the duty cycle D of the extended converter in the step-up operation. Under reverse circumstance, after sampling the voltage and the power of the PV and determining that the operating point is in the left side of the power-voltage characteristic curve shown in Figure 10, the proper command to the MPPT controller should be applied to increase the PV voltage or decrease the duty cycle D of the extended converter in the step-up operation.

Noted that the sampling process is accomplished by the blocks existed in PSCAD software. According to Figure 11, the corresponding commands developed in FORTRAN language for implementation of the incremental conduction algorithm with varying step are given in the following. This code can be run in the PSCAD environment.

```
IF (ABS($dV).lt.0.001.and.ABS($dP).lt.0.001) THEN
END IF
IF (ABS($dV).gt.0.001.and.ABS($dP).gt.0.001.and.$q.gt.0.and.q_1.gt.0) THEN
    $Dn=$D-0.05
ELSEIF(ABS($dV).gt.0.001.and.ABS($dP).gt.0.001.and.$q.gt.0.and.q_1.lt.0) THEN
    $Dn=$D-0.01
ELSEIF(ABS($dV).gt.0.001.and.ABS($dP).gt.0.001.and.$q.lt.0.and.q_1.lt.0) THEN
    $Dn=$D+0.05
ELSEIF(ABS($dV).gt.0.001.and.ABS($dP).gt.0.001.and.$q.lt.0.and.q_1.gt.0) THEN
    $Dn=$D+0.01
END IF
```

Figure 11 Incremental conduction approach with varying step flowchart

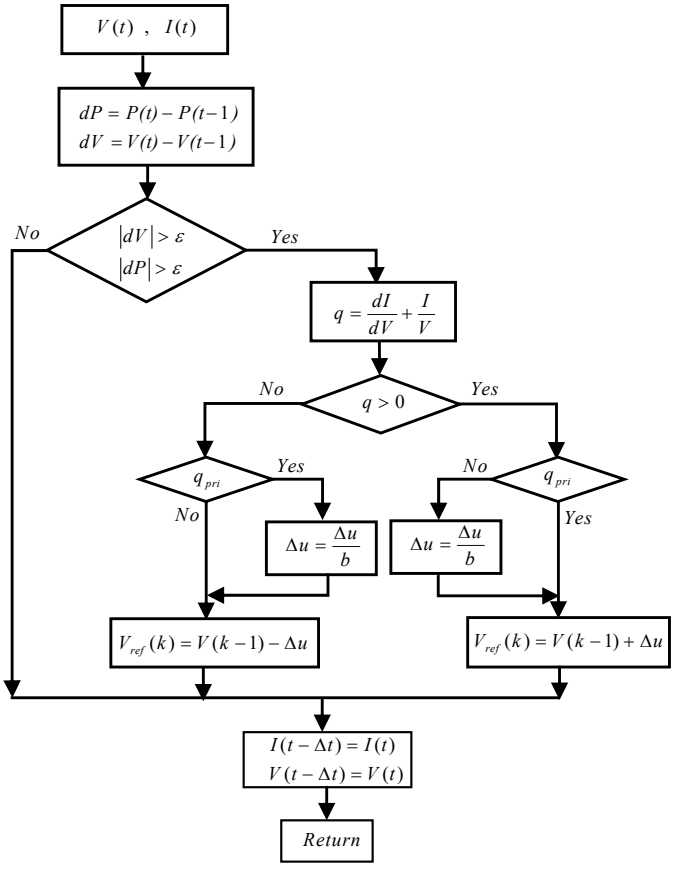

In the commands, dV is the output voltage difference of the PV system for the two consecutive samples. In similar manner, dP is the output power difference of the PV system for two consecutive samples.

The parameter D_n is the output duty cycle of the controller for triggering the DC-DC switches of the converter while D is the duty cycle of the extended converter in a previous sample. q and q_{-1} are the slope of the power-voltage characteristic curve in the two consecutive samples.

According to the flowchart depicted in Figure 11, the slope of the power-voltage characteristic curve of the PV system is defined as follows:

$$q = \frac{d\left(I_{pv}V_{pv}\right)}{V_{pv}dV_{pv}} = \frac{dI_{pv}}{dV_{pv}} + \frac{I_{pv}}{V_{pv}} \cong \frac{\Delta I_{pv}}{\Delta V_{pv}} + \frac{I_{pv}}{V_{pv}} \tag{88}$$

Having the slope of q and the slope of the power-voltage characteristic curve in a previous sample, cause that the magnitude of the disturbance step, which is applied to the duty cycle, would be flexible. This means that if for two consecutive sample, slope samples of q and q_{pri} are in the same direction, then the disturbance step is equal to Δu. Similarly, if the slope samples of q and q_{pri} are in opposite directions for the two consecutive samples, then the disturbance step is equal to $\Delta u / b$. This process is done for decreasing the magnitude of the oscillations around the maximum power point. In this regard, the quantity Δu, stands for to ΔD, i.e., the value of the disturbance which is applied to the duty cycle. Finally, the optimum value of the duty cycle D is applied to an appropriate comparator as an input and then compared with a triangular wave. The output of the comparator is the triggering signal associated with the switches of the converter. To clarify the MPPT control approach, the duty cycle of all the four switches are considered to be equal and, by referring to Figure 12, the phase shift of the triangular waves related to the switches is set equal to 90 degrees. The parameter θ_0 is the initial phase of the triangular signal. Figure 12 shows the process for generating the switches triggering pulses in which the value of the optimum duty cycle of the MPPT control block output is the duty cycle of the extended converter's switches. By using this approach at the time of MPPT extraction if the number of inputs increases to n stages, the phase shift equal to 360/n degrees is considered between the switches at the moment they begin to conduct.

Figure 12 Triggering pulses control of MPPT for the extended converter

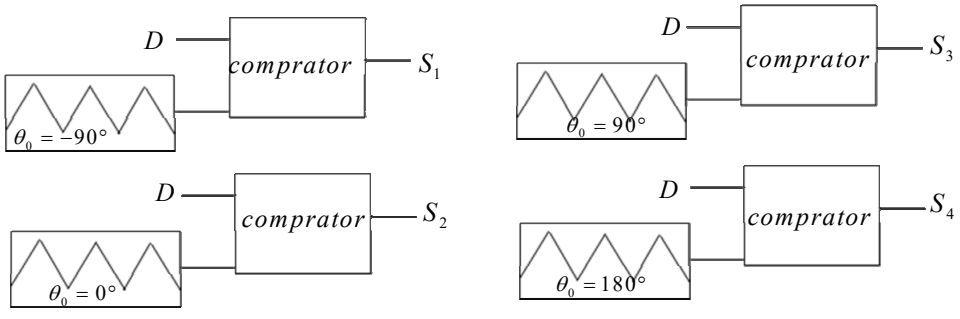

In step-down operation of the extended converter, after the sampling from the PV voltage and power, if it is determined that the operating point is on the right side of the

voltage-power characteristic curve shown in Figure 10, the command for decreasing the voltage of the PV or increasing the duty cycle D should be applied to the MPPT controller or, conversely, after the sampling from the PV voltage and power, if it is determined that the operating point is on the left side of the voltage-power characteristic curve shown in Figure 10, the command for increasing the voltage of the PV or decreasing the duty cycle D should be applied to the MPPT controller.

7 Experimental and simulation results

In this section, first the experimental results are provided for the four-port converter. Afterwards, the simulation results related to the MPPT will be demonstrated by PSCAD software for a PV system, which employs the proposed four-port converter in its configuration.

7.1 Experimental results for four-port converter

In this section, to verify the theoretical analysis of the extended converter, a 80W four-port converter was manufactured as a prototype in laboratory and the experimental results including the current and voltage of the switches, voltages and currents of input, and output voltage were provided. The parameter values used for the experimentation are listed in Table 2. The measured voltage and current waveforms of the extended converter are presented in Figure 13. One cycle of operation is highlighted in the figures. Some interpretations about the experimental results are given in the following.

It can be inferred from Figures 13(a) to 13(d) that in the first mode, the current of the switches S_1, S_2 and S_3 rise with positive slope as described by the relations (27), (26) and (25), respectively. It can be shown from Figure 13(d) that the current of S_4 is zero; because S_4 turns off in this mode as expressed in the first part of Section 4. In similar manner, in the second mode, the current of the switches S_1, S_2, and S_4 rise with positive slope as described by the relations (30), (29) and (28), respectively. It can be shown from Figure 13(c) that the current of S_3 is zero; because S_3 turns off in the second mode as expressed in the second part of Section 4.

In the third mode, the current of the switches S_1, S_3 and S_4 rise with positive slope as described by the relations (32), (31) and (33), respectively. It can be shown from Figure 13(b) that the current of S_2 is zero; because S_2 turns off in the third mode as expressed in the third part of Section 4. Similar interpretation can be expressed for the fourth mode which is omitted to conserve the space.

The negative sign of the currents i_{l1} and $_{l2}$ in Figures 13(e) and 13(f) show that at the low voltage side, which consists of V_{l1} and V_{l2}, the energy transfers to the output load. Regarding the Figure 13(h), the value for the voltage stress over the switch S_1 is equal to the high voltage side i.e., V_H in the fourth mode, in which the switch S_1 turn off. This issue is verified by referring the status of the circuit in fourth mode described in Section 4. With regards to Figure 13(i), Figure 13(j), the voltages in low voltage side, that is V_{l1} and V_{l2}, are almost 20^{v} and 40^{v} as expressed in Table 2. Similarly, the output voltage value for the high voltage side is found almost 80^{v} which is expressed by V_H in Table 2.

Figure 13 Experimental results of the four-port converter; (a) to (d) show the current of the switches; (e) to (g) show the input currents; (h) voltage of the switch S_1 (i) and (j) show the input voltages and (k) depicts the output voltage (see online version for colours)

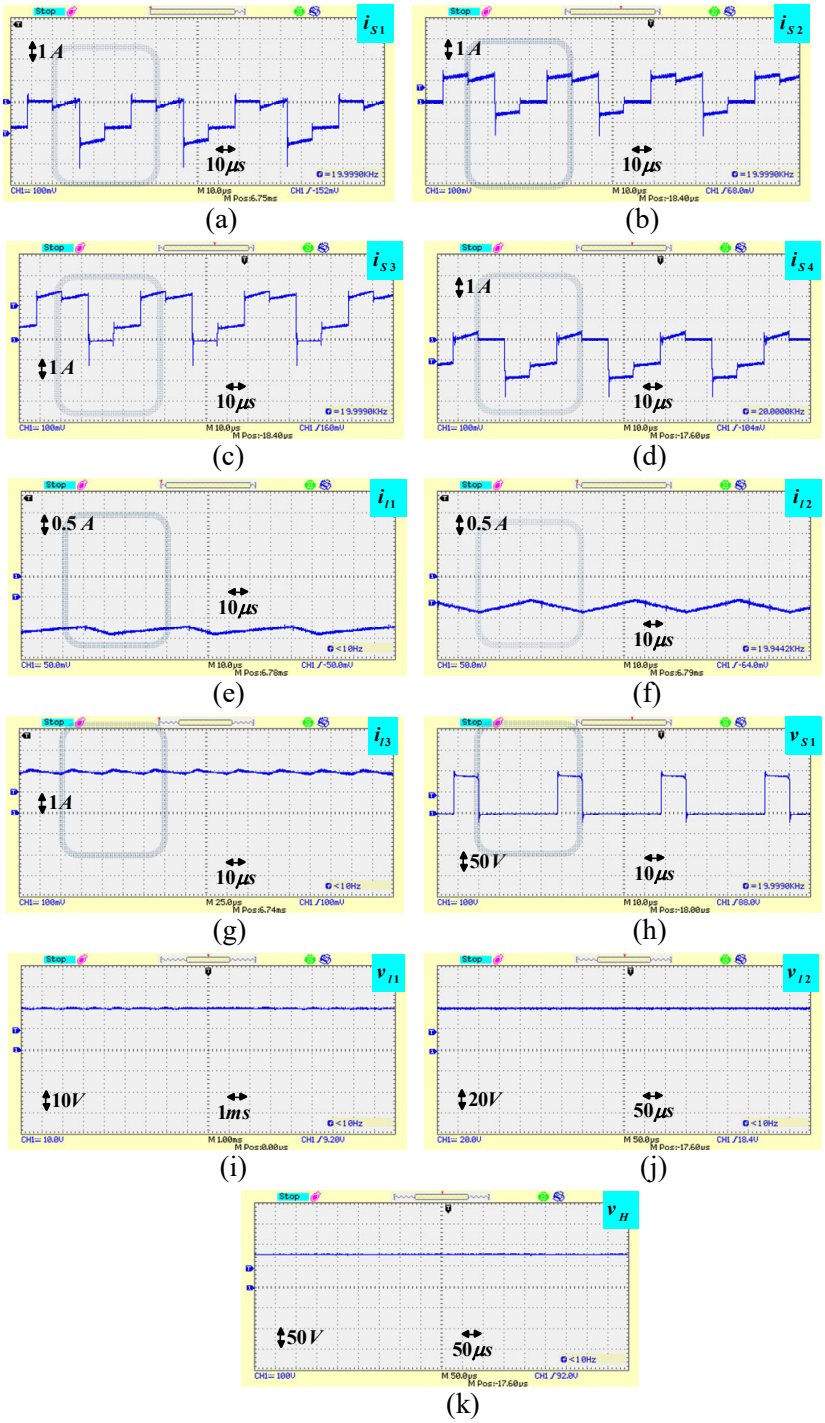

Table 2 Parameter values used for the experimentation of the four-port converter

$V_H = 80^v$, $V_{I1} = 20^v$, $V_{I2} = 40^v$, $V_{I3} = 60^v$	$f_s = 20$ kHz
$R_{I2} = 60\Omega$	$C_{I1} = C_{I2} = 50\ \mu F$
$R_{I1} = 15\Omega$	$L_1 = L_2 = L_3 = 4$ mH
Ch = 60 μF	$R_H = 100\Omega$
$D_3 = D_2 = D_1 = D_4 = 0.25$	

Figure 14 Simulation results of the converter by implementing the MPPT algorithm, (a) power (b) voltage of the PV system (c) duty cycle 1 – D (d) efficiency of the PV system (e) radiation in one period (see online version for colours)

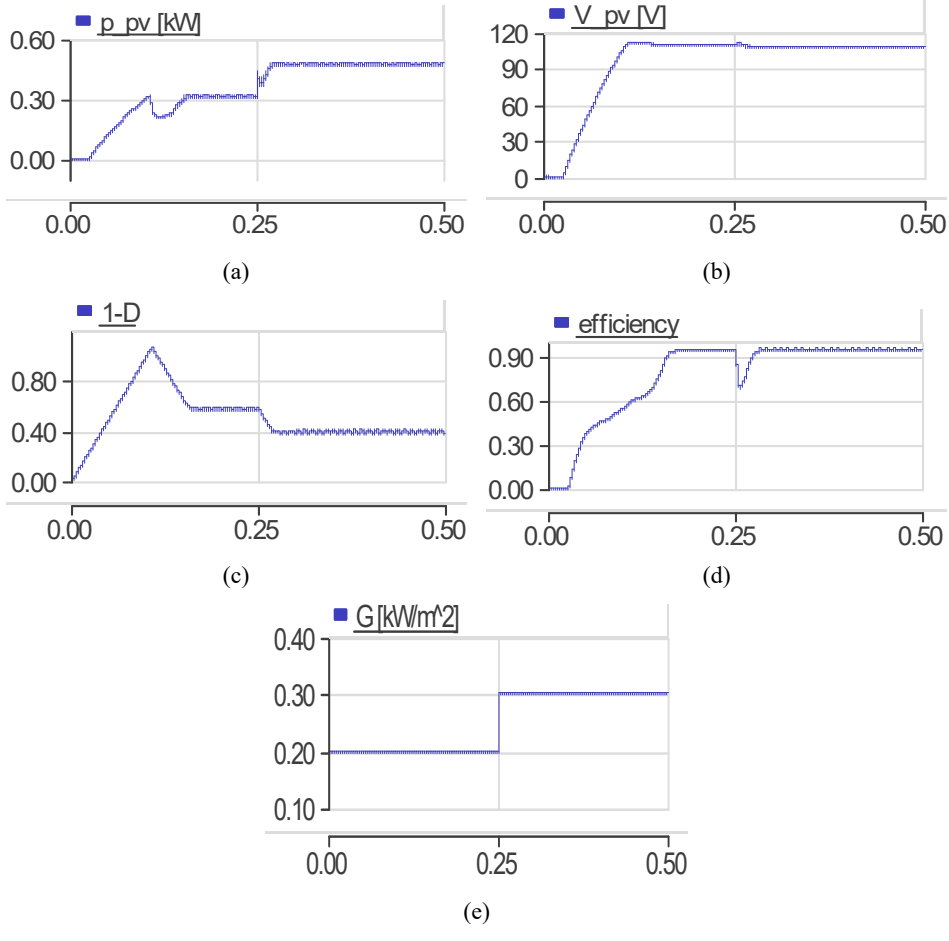

Note: The x-axes show the time in millisecond for all subfigures.

7.2 Simulation results

In this section, the PV system consisting of PV source, four-port converter, MPPT controller and output load is simulated in accordance with Figure 9. The parameter values

in the MPPT simulation are listed in Table 3. During the simulation, the temperature is kept unchanged for standard state at 298 K. Figure14 illustrates the simulated results for the power P_{PV}, voltage V_{PV}, duty cycle $1 - D$ and the efficiency of the PV system. These quantities are obtained for the extraction of maximum power from the extended converter under step variation of radiation from 200 W/m^2 to 300 W/m^2.

Given that the power P_{mpp} and the voltage V_{mpp}, which correspond to the maximum power point of characteristic curve shown in Figure 10, coincide with the simulated output power and voltage of the PV source under steady state operation (V_{PV}, P_{PV}) shown in Figure 14, it can be concluded that the implemented MPPT algorithm works well.

Figure 15 MPPT simulation results of the four-port converter (a) to (c) show the current of the switches (d) shows the input currents (e) depicts the voltage of the switch S_3 (f) shows the input and output voltages (see online version for colours)

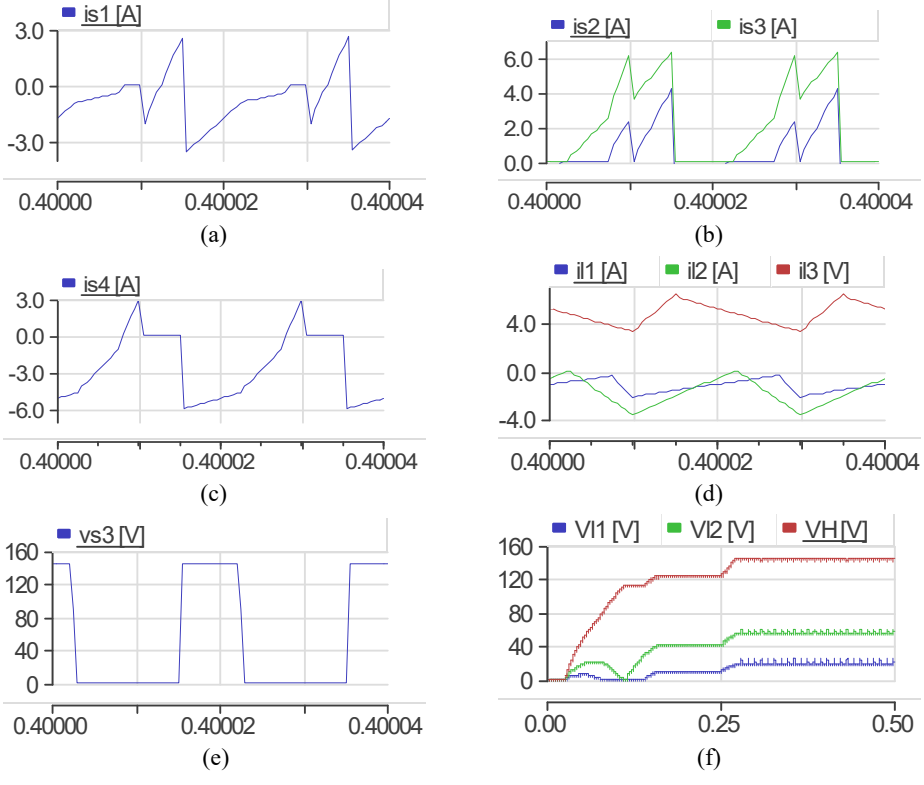

Moreover, regarding Figure 14, it can be observed that the voltage waveform of the PV source (V_{PV}) under steady state operation, has an approximately fixed DC component which shows that the MPPT is properly operating. In addition, the efficiency yielded from the PV system simulation is almost 95%. Figure15 demonstrates the MPPT simulation results, including the current of the switches and input and output voltages for the four-port converter with specifications listed in Table 3. It is worth mentioning that the PV source is substituted with the DC voltage level of V_{l3} for supplying three different output load of R_{l1}, R_{l2} and R_H. Similarly, the PV source can be substituted with each of the different DC voltage levels as V_{l1}, V_{l2} and V_H. As such, the maximum power of the PV system can be obtained.

Table 3 Parameter values used for simulating the MPPT

$V_H = 150^v$, $V_{l1} = 20^v$, $V_{l2} = 60^v$, $V_{l3} = 60^v$ $V_{l3} = 109^v$, (mono crystalline silicon 1.5^{kW}	$f_s = 20$ kHz
$R_{l2} = 30\Omega$	$C_{l1} = C_{l1} = 50\ \mu F$
$R_{l1} = 15\Omega$	$L_1 = L_2 = L_3 = 185\ \mu$H
$R_H = 60\Omega$	$C_H = 60\ \mu F$
$f_{sampler} = 2\ kHz$	

8 Conclusions

In this paper, an extendable *n*-port bidirectional DC-DC converter is analysed and implemented. The advantage of the improved topology is its simple configuration with reduced number of switches, capable of extending to any number of desirable ports, no need for passive equipment, and small size hanks to not to use transformer in the topology while keeping its operational performance. A complete design of a PV system consisting of PV modules, multiple-port DC-DC converter, MPPT controller and output loads with various voltage levels is implemented and simulated by PSCAD software under varying radiation conditions. Simulation efficiency of the PV system by utilisation of the extended converter under varying radiation conditions is achieved almost 95%. As a typical case, the operational performance of a four-port converter is validated through the experimental results.

References

Babaei, E., Abbasnezhad, A., Sabahi, M. and Hosseini, S.H. (2017a) 'Analysis and design of a soft-switching boost DC/DC converter', *IET Power Electronic*, Vol. 10, No. 11, pp.1353–1362.

Babaei, E. and Abbasi, O. (2015) 'Structure for multi-input multi-output DC-DC boost converter', *IET Power Electronic*, Vol. 9, No. 1, pp.9–19.

Babaei, E., Laali, S. and Bahravar, S. (2015) 'A new cascaded multi-level inverter topology with reduced number of components and charge balance control methods capabilities', *Electric Power Components and Systems*, Vol. 43, No. 19, pp.2116–2130.

Babaei, E., Saadatizadeh, Z, Mohammadi, M. and Mohammadi-ivatloo, B. (2017c) 'A new interleaved bidirectional zero voltage switching dc/dc converter with high conversion ratio', *Journal of Circuits, Systems, and Computers*, Vol. 26, No. 6, pp.1750105–25.

Babaei, E., Saadatizadeh, Z. and Cecati, C. (2017b) 'High step-up high step-down bidirectional DC/DC converter', *IET Power Electron*, Vol. 10, No. 12, pp.1556–1571.

Babaei, E., Saadatizadeh, Z., Mohammadi, M. and Mohammadi-ivatloo, B. (2017c) 'A new interleaved bidirectional zero voltage switching dc/dc converter with high conversion ratio', *Journal of Circuits, Systems, and Computers*, Vol. 26, No. 6, pp.1750105–25.

Bahravar, S., Babaei, E. and Hosseini, S.H. (2012a) 'New cascaded multilevel inverter topology with reduced variety of magnitudes of DC voltage sources', *IEEE Int. Conf. Power Electron. (IICPE)*, pp.1–10.

Bahravar, S., Mahery, H.M., Babaei, E. and Sabahi, M. (2012b) 'Mathematical modeling and transient analysis of DC-DC buck-boost converter in CCM', *IEEE International Conference on Power Electronics (IICPE)*, Delhi, India, pp.1–10.

Behjati, H. and Davoudi, A. (2013) 'Single-stage multi-port DC-DC converter topology', *IET Power Electronic*, Vol.6, No. 2, pp.392–403.

Deihimi, A., Mahmoodieh, M.E. and Iravani, R. (2017) 'A new multi-input step-up DC-DC converter for hybrid energy systems', *Electric Power Systems Research*. Vol. 149, pp.111–124.

Dhananjaya, M. and Pattnaik, S. (2019) 'Design and implementation of a SIMO DC-DC converter', *IET Power Electronics*, Vol. 12, No. 8, pp.1868–1879.

Dos Santos, E.C. (2013) 'Dual-output DC-DC buck converters with bidirectional and unidirectional characteristics', *IET Power Electronic*, Vol. 6, No. 5, pp.999–1009.

Esram, T. and Chapman, P.L. (2007) 'Comparison of photovoltic rry mximum power point trcking techniques', *IEEE Transactions on Energy Conversion,* Vol. 22, No. 2, pp.439–449.

Farakhor, A., Abapour, M. and Sabahi, M. (2019) 'Design, analysis, and implementation of a multiport DC-DC converter for renewable energy applications', *IET Power Electronics*, Vol. 12, No. 3, pp.465–75.

Forouzesh, M., Shen, Y., Yari, K., Siwakoti, Y.P. and Blaabjerg. F. (2018) 'High-efficiency high step-up dc-dc converter with dual coupled inductors for grid-connected photovoltaic systems', *IEEE Transactions on Power Electronics*, Vol. 33, No. 7, pp.5967–5982.

Immanuel, T.B., Suresh, A. and Rashmi, M.R. (2016) 'A multi input multi output converter for hybrid energy systems', *Circuits and Systems*', Vol. 7, No. 6, pp.771–778.

Jalihal, D., Jhunjhunwala, A. and Kaur, P. (2018) 'Solar-DC micro-grids for multi-storied building complexes in emerging nations', *International Journal of Power Electronics*, Vol. 9, No. 3, pp.274–286.

Jayasankar, V.N. and Vinutha, U. (2018) 'Design of backstepping controller for PV-wind hybrid system with grid-interfacing and shunt active filtering functionality', *International Journal of Power Electronics*, Vol. 9, No. 2, pp.167–188.

Kardan, F, Alizadeh, R. and Banaei, M.R. (2017) 'A new three input DC/DC converter for hybrid PV/FC/battery applications', *IEEE Journal of Emerging and Selected Topics in Power Electronics*, Vol. 5, No. 4, pp.1771–1778.

Katayama, N., Tosaka, S.H., Yamanaka, T., Hayase, M., Dowaki, K. and Kogoshi, S. (2016) 'New topology for DC-DC converters used in fuel cell-electric double layer capacitor hybrid power source systems for mobile devices', *IEEE Transactions on Industry Applications*, Vol. 52, No. 1, pp.313–321.

Khosrogorji, S., Ahmadian, M., Torkaman, H. and Soori, S. (2016) 'Multi-input DC/DC converters in connection with distributed generation units – a review', *Renewable and Sustainable Energy Reviews*, Vol. 66, pp.360–379.

Kunalkumar, B., Gupta, R.A. and Gupta, N. (2019) 'Design and simulation of bi-directional DC-DC converter with dual switch forward snubber', *International Journal of Power Electronics*, Vol. 10, Nos. 1/2, pp.82–101.

Mohseni, P., Hosseini, S.H., Sabahi, M., Jalilzadeh, T. and Maalandish, M. (2018) 'A new high step-up multi-input multi-output DC-DC converter', *IEEE Transactions on Industrial Electronics*, Vol. 66, No. 7, pp.5197–208.

Nathan, K., Ghosh, S., Siwakoti, Y. and Long, T.A. (2018) 'New DC-DC Converter for PV systems: coupled-inductors combined Cuk-SEPIC converter', *IEEE Transactions on Energy Conversion*, Vol. 34, No. 1, pp.191-201.

Rahman, S.A. (2012) *Novel Controls of PV Solar Farms*, PhD thesis, The University of Western Ontario, Canada.

Rehman, Z., Al-Bahadly, I. and Mukhopadhyay, S. (2015) 'Multi input DC-DC converters in renewable energy applications – an overview', *Renewable and Sustainable Energy Reviews*, Vol. 41, pp.521–539.

Shahir, F.M., Babaei, E. and Farsadi, M. (2017) 'A new structure for non-isolated boost DC-DC converter', *Journal of Circuits, Systems, and Computers*, Vol. 26, No. 1, pp.1750012 (1–26).

Wai, R.J. and Zhang, Z.F. (2019) 'High-efficiency single-input triple-outputs DC-DC converter with zero-current switching', *IEEE Access*, Vol. 7, pp.84952–84966.

Wang, Z. and Li, H. (2013) 'An integrated three-port bidirectional DC-DC converter for PV application on a DC distribution System', *IEEE Transactions on Power Electronics*, Vol. 28, No. 10, pp.4612–4624.

Wu, Y.E. and Chen, I.C. (2019) 'Novel integrated three-port bidirectional DC/DC converter for energy storage system', *IEEE Access*, Vol. 7, pp.104601–104612.